PAPER

Check for updates

Physical properties of Fe-doped CdS quantum dots: single dot rectifying diode application

Piyali Maity, †[a] Ravi Kumar,[b] S. N. Jha,[b] D. Bhattacharyya,[b] Sandip Chatterjee,[c] Bhola Nath Pal[d] and Anup Kumar Ghosh *[a]

The domain of single-molecule based electronic devices has grown remarkably over the past decade by utilizing nanotechnology to improve the efficiency of device fabrication. However, most of the single-molecule devices are based on organic materials. Compared with organic molecules, quantum dots (QDs) are excellent owing to their crystalline nature, environmental stability, narrow emission band and quantum yield with tunable electronic and optoelectronic properties. Here, CdS:Fe QDs were synthesized and analyzed to assess their structural, optical, and electronic properties, and subsequently, they were implemented in fabricating single-dot rectifying diodes. EXAFS revealed the average coordination number of the doped Fe element. The ITO/TiO$_2$/CdS:Fe quantum dot heterostructure rectifying diodes were grown by spin coating and were characterized using scanning tunneling microscopy (STM) at room temperature. STM images revealed the distribution of QDs over the substrate, and the spectra revealed the improved rectification behavior with tunneling up to ~1000×, revealing their excellent diode functionality. Threshold voltage tuning from 1.62 eV to 0.83 eV indicated the application of these diodes for tunable electronics with low power consumption. Thus, these results indicate the promising use of CdS:Fe QDs for optimized ambient atmosphere rectifying diode applications, opening the way for innovative electronic devices with improved performance and functionality.

1. Introduction

Semiconductor technology is an essential part of modern life. Developments in microfabrication and optoelectronics are crucial for enabling advanced technologies in semiconductor industries. In recent decades, the use of electronic devices has massively expanded. This transformation has been made possible by the impressive developments in the fabrication and miniaturization of the active components of electronic devices. According to Moore's law, rapid miniaturization requires modern technologies.[1] Miniaturization technologies focus on developing quantum-sized devices with little power consumption and low-cost market price. Single-molecule electronics have been explored for several decades as one of the possible routes for electronic devices. For example, single-

molecule or single-dot devices with advanced functions such as molecular switches,[2–4] single molecule diodes with high rectification,[5–7] and single atom transistors[8] have been fabricated. However, fabrication, reproducibility, and stability remain critical issues for single-molecule electronic devices. This could be resolved using single quantum dot semiconductor materials. CdS quantum dots (QDs) significantly compel electronic functions to make single-dot electronic devices.[9–11] Quantum dots can enable the fabrication of highly efficient single-dot electronic devices. This work concentrates on the synthesis and characterization of self-assembled monolayer rectifying devices with a single QD or a small number of QDs.[12–14]

The development of silicon-based electronic devices is becoming limited. Single-molecule electronic devices, which are getting more attention, are considered one of the most promising candidates to achieve the miniaturization of conventional electronic devices. Molecular-sized electronic devices must be miniaturized and integrated as much as possible to reduce power consumption. The performance of molecular electronic devices is based on the quantum confinement effect of electrons, which is different from traditional electronic devices. The semiconductor quantum dots based conventional electronic devices will gain enormous popularity.[15–17] Therefore, our low threshold

[a] Department of Physics, Institute of Science, Banaras Hindu University, Varanasi, India. E-mail: akghosh@bhu.ac.in; Tel: +91 542 6701556

[b] Atomic & Molecular Physics Division, Bhabha Atomic Research Centre, Mumbai, India

[c] Department of Physics, Indian Institute of Technology (Banaras Hindu University), Varanasi, India

[d] School of Materials Science and Technology, Indian Institute of Technology (Banaras Hindu University), Varanasi, India

† Present address: City University of New York, 695 Park Ave, New York, NY 10065, USA.

voltage rectifying diode is a possible solution. While remarkable advancements have been made in single-nanostructure devices and single organic molecule devices, there is a requirement for single quantum dot (QD)-based devices. This study aims to advance single nanoparticle or molecule nanoelectronics by reducing device size and enhancing performance. Colloidal quantum dots are promising materials due to their tunable physical properties, environmental stability, and advanced optoelectronic properties compared to organic molecules. This study aims to explore the single-dot electronic devices by rectifying diodes with high performance and low external power. Although there are many reports on CdS QDs and their applications, to the best of our knowledge, there is no report on Fe-doped CdS QDs thin film rectifying diodes. Various approaches to build and study the molecular junctions have been developed,[18,19] including mechanically controllable break junctions (MCBJs),[20,21] conductive atomic force microscopy electron migration scanning tunneling microscopy (STM) junctions,[8,22–26] oxidative lithography[27,28] or self-assembled methods,[29] thermally evaporated and deposited metal film,[30] and large-area molecular junctions.[31] These techniques enable the probing of charge transport at the molecular and electronic levels.[32–35] Because charge transport in single-dot junctions is quantum mechanical, molecular electronics offer unique opportunities for the discovery of fundamental physical phenomena and for the direct observation of effects that are not accessible in bulk materials. These effects include quantum interference (QI),[36–38] the Coulomb blockade, and the Kondo effect. Moreover, devices with various remarkable functions such as single-molecule switches,[4,39,40] molecular thermos-electronic devices,[41,42] single-molecule diodes,[43] single-molecule spintronic devices[44,45] and sensors with single-molecule sensitivity[46–49] have been explained within molecular junctions. An excellent imaging method for a broad range of possibilities for real space imaging on a scale that extends to atomic dimensions can be developed by STM and electrical property-related information can be obtained by this process.[50,51]

However, the implementation of techniques that are capable of atomic resolution, such as STM are needed to gain a profound dominance of the junction geometry in molecular-level experiments. Indeed, the possibility of incorporating an electrode within the STM geometry can favorably complement its high lateral resolution, giving an additional possibility of tuning the electronic properties of nanomaterial accessible by STM.[52–57]

This work discusses the tuned structural-, optical-, and electronic properties of iron (Fe) doped CdS quantum dots have been discussed. The synthesized quantum dots have been used to fabricate low threshold voltage thin film single dot rectifying diodes which will be useful as a switch or rectifier in day-to-day life. The importance of this study is the fabrication of single QD-based rectifying diodes that operate in ambient atmospheric conditions. Typically, single particle/

molecule-based devices are studied by ultra-high vacuum STM studies. Meanwhile, this work demonstrates the operation of a device in open atmospheric conditions. In addition, the variable Fe-doping in CdS QDs helps to tune the threshold voltage, which plays an important role for practical applications. Moreover, this study used a simple fabrication technique (spin coating) and measurement techniques at ambient condition (STM) to fabricate and study single dot rectifying diodes. Iron (Fe) doping significantly enhanced the rectification behavior and reduced the threshold voltage, with potential development of advanced electronic systems with minimal electrical power loss.

2. Experimental details

For the synthesis of Fe-doped CdS quantum dots $Cd_{1-x}Fe_xS$ ($0 \leq x \leq 0.08$), the precursors cadmium acetate di-hydrate, iron nitrate nano-hydrate, and sodium sulfide were used. The samples were prepared by the hot injection methods under an argon atmosphere at 100 °C for 12 h. Cadmium acetate di-hydrate and iron nitrate nano-hydrate were mixed in dimethyl sulfoxide solvent for 20 min. After that, a purged aqueous solution of sodium sulfide was added and mixed until the homogeneous solution was obtained. Then, 1-mono thioglycerol was added as a ligand. The solution was refluxed at 100 °C for 12 h. Then, the solution was cooled down to room temperature and washed with acetone and methanol. The yellow precipitate was collected and dried in vacuum.[58] The synthesized quantum dots were characterized by X-ray diffraction (XRD), transmission electron microscopy (TEM), Raman spectroscopy, UV-vis spectroscopy, and photoluminescence spectroscopy (PL). The composition of $Cd_{1-x}Fe_xS$ was calculated according to the stoichiometric ratio. Subsequently, the samples were prepared by adding the precursors stoichiometrically. The best fitted curve of Rietveld refinement of the XRD data confirm the composition of the materials. This also provides information on structural changes due to Fe incorporation. During the experiment, the doping process was precisely controlled to ensure uniformity and reproducibility of iron doping into the CdS. Multiple synthesis trials were performed, and the iron doping concentration was consistent across different batches.

For the rectifying diode fabrication, the isopropanolic solution of TiO_2 nanopowder (Sigma Aldrich) was coated on the cleaned surface of indium tin oxide (ITO) and heated at 350 °C for 30 min. Then, the single layer Fe-doped CdS quantum dots isopropanolic solution (1 mg/2 ml) was spin-coated at 1500 rpm. For characterization of the fabricated devices, scanning tunneling microscopy (STM) was performed in an ambient atmosphere. The devices were kept in vacuum until STM characterization.

The average crystallite sizes, D, of the samples are estimated from Debye–Scherrer's equation with X-ray diffraction data:

$$D = \frac{0.9\lambda}{\beta \cos\theta} \tag{1}$$

© 2025 The Author(s). Published by the Royal Society of Chemistry

RSC Appl. Interfaces, 2025, **2**, 952–964 | **953**

where λ is the wavelength of the radiation used (λ = 1.5406 Å), β is the full width at half maxima (FWHM), and θ is the Bragg angle.

The lattice parameter ($a = b = c$) was estimated from Rietveld refinement of the X-ray diffraction data and by using the following formula:

$$\sin^2 \theta = \frac{\lambda^2}{4} \frac{h^2 + k^2 + l^2}{a^2} \qquad (2)$$

where θ is the angle of diffraction, λ is the incident wavelength (λ = 1.5406 Å), and h, k, and l are Miller indices.

The linear increase of the 'a' parameter can be explained based on the micro-strain developed due to Fe-doping. The micro-strain was calculated using the following equation:

$$\delta = \frac{\beta \cos \theta}{4} \qquad (3)$$

where β is the FWHM, and θ is the corresponding diffraction angle.

3. Results and discussion

3.1. X-ray diffraction (XRD) study

XRD measurements were performed for structural analysis of the prepared samples. The Rietveld refinement profiles of the prepared samples are shown in Fig. 1. Three prominent intense peaks at 2θ = 26.82°, 43.94°, and 51.86° corresponding to (111), (220), and (311) planes, respectively, confirm the cubic phase of CdS (JCPDS file #10-0454). All peak positions of undoped and Fe-doped CdS corresponding to the standard Bragg peaks of the zinc blende cubic structure are shown by the vertical bars, and the residue is represented by the line, respectively, at the bottom of the

XRD patterns. The XRD patterns show that there is no appearance of any extra peaks or disappearance of any peak in the zinc blende structure of undoped CdS due to Fe doping. This confirms that the structure of the Fe-doped CdS in the zinc blende phase belongs to the $F\bar{4}3m$ space group. This analysis reveals that the samples are single-phased, having no trace of impurities. The well doped and crystalline structure was further confirmed by extended X-ray absorption fine structure spectroscopy (EXAFS). The close observation shows that the peak intensity for (111) peak decreases slightly with an increased doping concentration. The gradual decrement of the peak height with increasing Fe-concentration signifies the incorporation of Fe ions into the Cd-sites. The incorporation of Fe ions into the Cd-sites creates very small local distortion into the crystals (as observed from Raman spectra analysis) which causes a decrease in the peak height.[58,59]

Variation of the average crystallite size with the Fe-doping concentration is depicted in Fig. 2a. The average crystallite size decreases linearly with the doping concentration. This result can be explained by the mechanism of growth kinetics. The chemical reactions follow two steps. In the first step, nucleation and interactions among the nucleation take place to reach the critical size. In the second step, these critical sizes grow into nanocrystals. The growth rate and the size can be explained based on the binding energy of the bonds.[60]

The lattice parameters (a) have been estimated from Rietveld refinement and using eqn (2). The variation of 'a' with Fe-concentration (x) has been plotted in Fig. 2b, which shows that there is a small increase in the lattice parameter 'a' due to the increase of Fe-ion doping. A small increase in 'a' with Fe-doping cannot be attributed to the difference in ionic radii between divalent Fe (0.78 Å) and divalent Cd (0.96 Å) in tetrahedral coordination. It should be expected that the substitution of Cd^{2+} by Fe ions may lead to a decrease in the lattice parameters due to a smaller ionic radius of divalent Fe in tetrahedral coordination. Thus, the linear increase of the 'a' parameter cannot be explained by the difference in ionic radii. Moreover, linear variation of lattice constant 'a' with increasing Fe-concentration confirms that the Fe-ion has been substituted into the crystal lattice following Vegard's law. It also confirms that this is no structural change, and the doping of Fe-ions does not change the zinc blende structure of CdS. The variation of micro-strain with Fe concentration is plotted in Fig. 2c.

The XRD results reveal that the samples are cubic zinc blende in nature with broadening in the peaks due to their small size.[58,59] The broadening increases with the doping concentration due to the decreasing size of the quantum dots with Fe doping concentration (Fig. 2d). This may be attributed to the quantum confinement effect, surface defect, and dopant induced strain;[60,61] therefore, it is desirable to tune the efficiency of the single-dot-devices. The replacement of Cd with Fe during doping changes the lattice parameters and bond lengths of the CdS quantum dots, which results in the change in structural properties. The value of the average
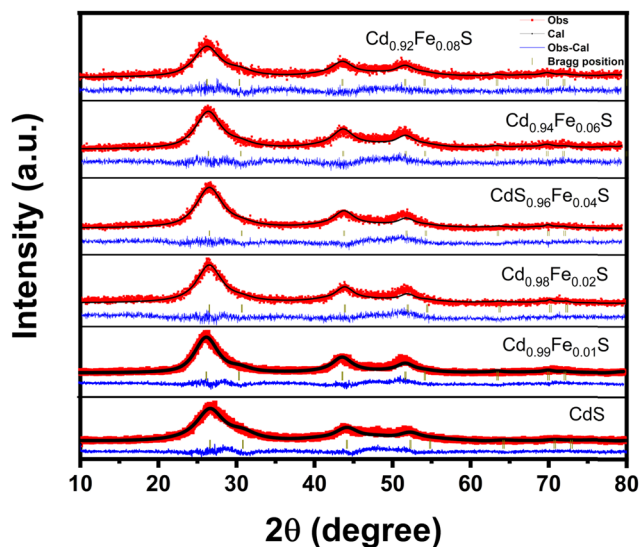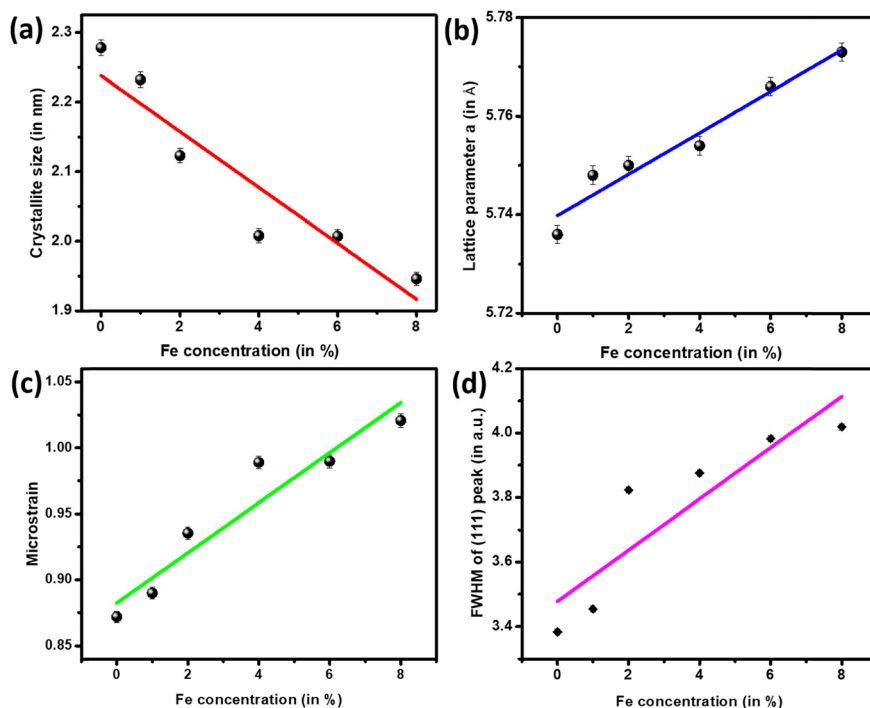

Fig. 1 Rietveld refinement profiles of X-ray diffraction (XRD) data of undoped and Fe-doped CdS quantum dots [$Cd_{1-x}Fe_xS$, Fe = 0, 0.01, 0.02, 0.04, 0.06, and 008]. The experimental data are represented by 'Obs', and the theoretical fit by Rietveld refinement is represented by 'Cal'.

Fig. 2 (a) Average crystallite size variation, (b) variation in lattice parameter 'a', (c) variation in micro-strain, (d) variation in FWHM of peak (111) with varying Fe doping concentration in CdS QDs. The crystallite size is decreasing with increasing doping concentration owing to quantum confinement.

Table 1 Crystallite size, lattice constant, lattice parameter, and micro-strain of CdS, $Cd_{0.99}Fe_{0.01}S$, $Cd_{0.98}Fe_{0.02}S$, $Cd_{0.96}Fe_{0.04}S$, $Cd_{0.94}Fe_{0.06}S$, and $Cd_{0.92}Fe_{0.08}S$ estimated from Rietveld refinement

Sample	Position (2θ)	Average crystallite size (in nm)	d spacing (in Å)	Lattice parameter a (in Å)	Micro-strain
CdS	26.887	2.278	3.312	5.736	0.87171
$Cd_{0.99}Fe_{0.01}S$	26.831	2.232	3.318	5.748	0.88976
$Cd_{0.98}Fe_{0.02}S$	26.822	2.123	3.319	5.750	0.93536
$Cd_{0.96}Fe_{0.04}S$	26.802	2.008	3.322	5.754	0.98884
$Cd_{0.96}Fe_{0.06}S$	27.155	2.007	3.329	5.766	0.98962
$Cd_{0.96}Fe_{0.08}S$	27.290	1.946	3.333	5.773	1.02066

crystallite size, lattice constant (d), lattice parameter ($a = b = c$), and micro-strain are shown in Table 1.

3.2. Transmission electron microscopy (TEM)

A low-resolution transmission electron micrograph shows that the average grain size of the samples is 2 nm (Fig. 3a). The TEM result corroborates with the XRD measurement. Both the average crystallite size estimated from the XRD and the average grain size estimated from the TEM measurement are less than the Bohr radii of CdS (~5.8 nm). From the low-resolution transmission electron micrograph, the monodispersive nature of the quantum dots has been observed, which is desirable in device fabrications. The irregular morphology in the TEM images can be attributed to the influence of the Fe doping. Fe is a transition metal and induces magnetism in the QDs after doping. The magnetism leads to jittering and distortion in the TEM images, which

may affect the clarity of the morphology of the QDs. The selected area electron diffraction (SAED) pattern of 2% Fe-doped CdS quantum dots (Fig. 3b) reveals that the samples are polycrystalline in nature.[58] The *hkl* values of planes are well matched with those of XRD measurements.

3.3. EXAFS spectroscopy

The X-ray absorption fine structure spectroscopy (XAFS) analysis of iron (Fe) doped cadmium sulfide (CdS) quantum dots was carried out at the Energy Scanning EXAFS beamline (BL-9) within the energy range of 4 keV to 28 keV located at the Indus-2 Synchrotron source (2.5 GeV, 100 mA) on the cadmium (Cd) and iron (Fe) K-edges. The optical system includes a rhodium/platinum (Rh/Pt) coated collimating meridional cylindrical mirror, which reflects the collimated beam. This beam is then monochromatized using a silicon (Si) (111) double crystal monochromator (DCM) with a lattice
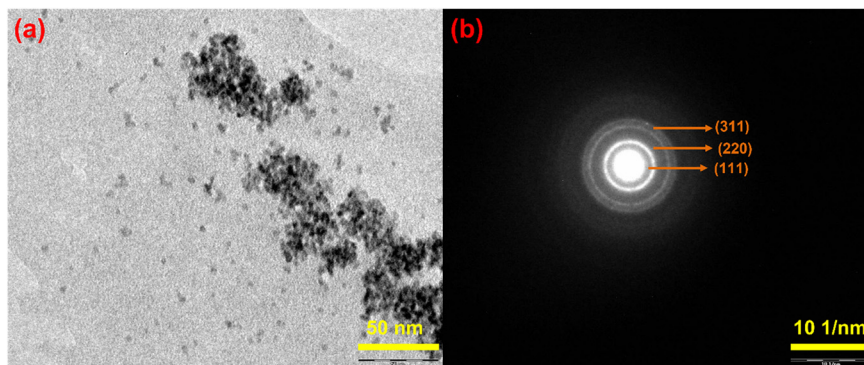
Fig. 3 (a) Low resolution transmission electron microscopic image and (b) SAED pattern of 2% Fe-doped CdS quantum dots.

spacing of 6.2709 Å. The second crystal of DCM is a sagittal cylinder utilized for horizontal beam focusing, while a downward-facing, Rh/Pt coated, bendable post mirror is employed for vertical beam focusing on the sample. To eliminate higher harmonic content in the X-ray beam, the second crystal of the DCM is detuned. X-ray absorption spectroscopy (XAS) measurements were carried out in both fluorescent and transmission modes.[62,63]

EXAFS data analysis requires background subtraction and normalizing the results followed by theoretical EXAFS calculations based on one or more chosen structural models. The best match was obtained by comparing the calculated spectra with the actual data are and the parameters were refined. In the fluorescence mode, the sample is positioned at an angle of 45° to the incoming incident X-ray beam. A fluorescence detector is then strategically placed perpendicular to the direction of this incident beam to capture the emitted signals. To quantify the incident beam flux, an ionization chamber detector is situated before the sample. The fluorescence detector records the emitted fluorescence intensity. In the transmission measurement method, three ionization chambers (length of 300 mm) are employed for data collection. The first ionization chamber is used to measure the incident beam flux, the second one is used to gauge the transmitted beam flux, and the third chamber is used to record the X-ray absorption spectrum of a reference metal foil for the purpose of energy calibration. To optimize the signal-to-noise ratio (SNR), specific gas pressures and gas mixtures are selected.

Cd K-edge. The normalized XANES spectra of above synthesized quantum dots measured at Cd K-edge are shown in Fig. 4a. The XANES spectra shows that the absorption edge positions of Cd in Fe-doped CdS almost coincide, which implies a similar oxidation state. The normalized absorption spectra of all samples are shown in Fig. 4b at the Cd K-edge. The EXAFS data were analyzed by the Demeter software package. This helps in reducing the background. Fourier transform of the absorption spectra was used to derive the $\chi(R)$ *versus* R plots using ATHENA software. The process involves the generation of theoretical EXAFS spectra starting from an assumed crystallographic structure and subsequently

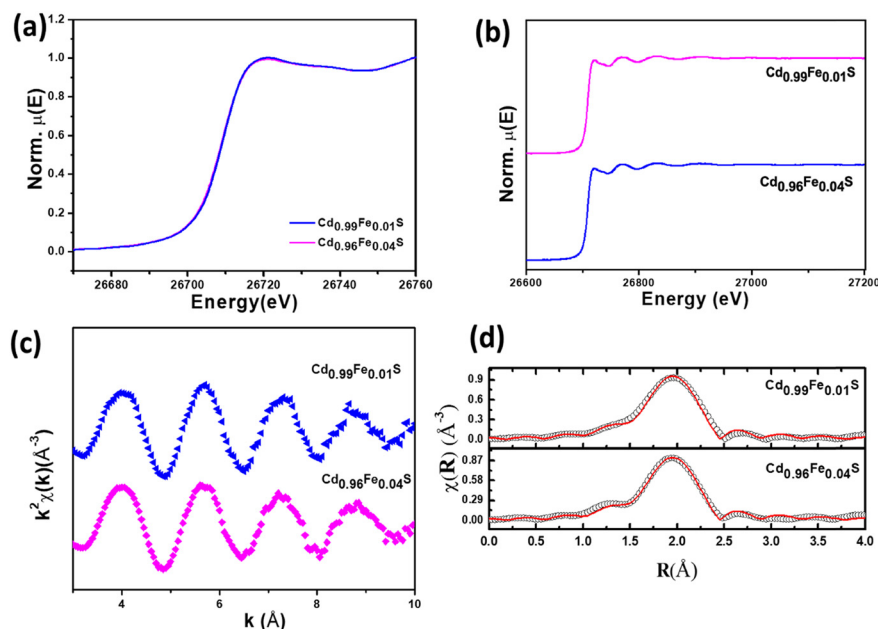fitting the experimental data with the theoretical spectra using ARTEMIS software for a detailed analysis.

Fig. 4c shows the $k^2\chi(k)$ *vs.* k spectra while the $\chi(R)$ *vs.* R plots are shown in Fig. 4d for the Cd K-edge of the synthesized Fe-doped CdS quantum dots. The $\chi(R)$ *vs.* R data of these samples have been fitted by assuming the cubic structure of the CdS crystal. In the fitting process, the coordination number (C.N.), atom-to-atom bond distance (R), and the disorder factor (Debye–Waller factor) (σ^2), which gives the mean square fluctuation in the atomic bond lengths and the thermal disorder in the system, have been used as fitting parameters and the best fit parameters are shown in Table 2. The contribution of the Cd–S coordination shell is confirmed by the presence of a peak at 2.0 Å in the radial distribution.[64,65]

Fe K-edge. The normalized XANES spectra of iron (Fe) doped CdS quantum dot samples shows the oxidation state of Fe in the samples (Fig. 5a). The normalized absorption spectra of $Cd_{0.99}Fe_{0.01}S$ and $Cd_{0.96}Fe_{0.04}S$ are shown in Fig. 5b. The $k^2\chi(k)$ *vs.* k spectra of the samples and $\chi(R)$ *vs.* R plots at the Fe K-edge are shown in Fig. 5c and d, respectively. The EXAFS data were initially fitted by considering Fe atoms at the Cd atomic positions in CdS after doping. The peak at 1.4 Å has contributions of two Fe–S coordination shells and the peak at 2.6 Å has contributions of the Fe–Fe coordination shell (Fig. 5d). The best parameters have been analyzed and shown in Table 3.

3.4. Raman spectroscopy

Raman spectroscopy has been employed to investigate the local structure, vibrational modes and defect-oriented local disorders present in samples. An excitation of 532 nm using a laser has been used to record the Raman spectra at room temperature for undoped and Fe-doped CdS quantum dots in the spectral range of 200–1500 cm^{-1}. CdS possesses the zinc blende cubic structure with space group $F\bar{4}3m$. Raman spectra of $Cd_{1-x}Fe_xS$ QDs show that the prominent peaks relate to confined longitudinal optical (LO) phonon modes, and their overtones (2LO and 3LO) are clearly observed for undoped and Fe-doped CdS QDs (Fig. 6a). Three prominent

Fig. 4 (a) Normalized XANES spectra, (b) normalized absorption spectra, (c) normalised EXAFS ($k^2\chi(k)$ vs. k) spectra, and (d) Fourier-transformed EXAFS spectra of $Cd_{0.99}Fe_{0.01}S$ and $Cd_{0.96}Fe_{0.04}S$ quantum dots at the Cd K-edge. In (d), the black colored scatter points represent experimental spectra, and the red colored solid line represents the theoretical fit.

peaks are located at 294, 588, and 885 cm^{-1} (Table 4), which correspond to the fundamental peaks related to stretching vibrations of LO phonon modes of 1LO, 2LO, and 3LO, respectively.[58] For all optical modes, characteristic Raman peaks may be attributed to (i) the optical phonon confinement effect for the lower frequency mode[66,67] and (ii) the surface optical (SO) phonons of spherical QDs,[68] as evidenced by TEM. The magnified image of the 1LO peak of different Fe-doping shows that the peak position shifts towards higher values with increasing Fe concentration (Fig. 6b). This type of shifting can be explained on the basis of the Heisenberg uncertainty relation:

$$\Delta p \Delta x \geq \hbar^2/4 \tag{4}$$

where Δx is the uncertainty in position, Δp is the uncertainty in momentum and $\hbar = h/2\pi$ is the reduced Planck's constant. XRD measurements show that the crystallite/particle size decreases with an increase in Fe-concentration. The phonon is confined in a smaller Δx region and there must be an increase in Δp with a decrease in crystallite size. The wave number distribution

also increases due to increase in momentum distribution of phonon (Δp), which causes the shift of the Raman peaks. Therefore, it can be concluded that the effect of phonon confinement may be responsible for the shifting of the Raman peak as discussed above in nano-sized crystallites. The confined LO phonon mode in spherical QDs has been extensively studied with the Gaussian confinement model.[69,70] According to this model, an optical phonon weighting function $W(r)$ in a small finite-sized crystal is given by:
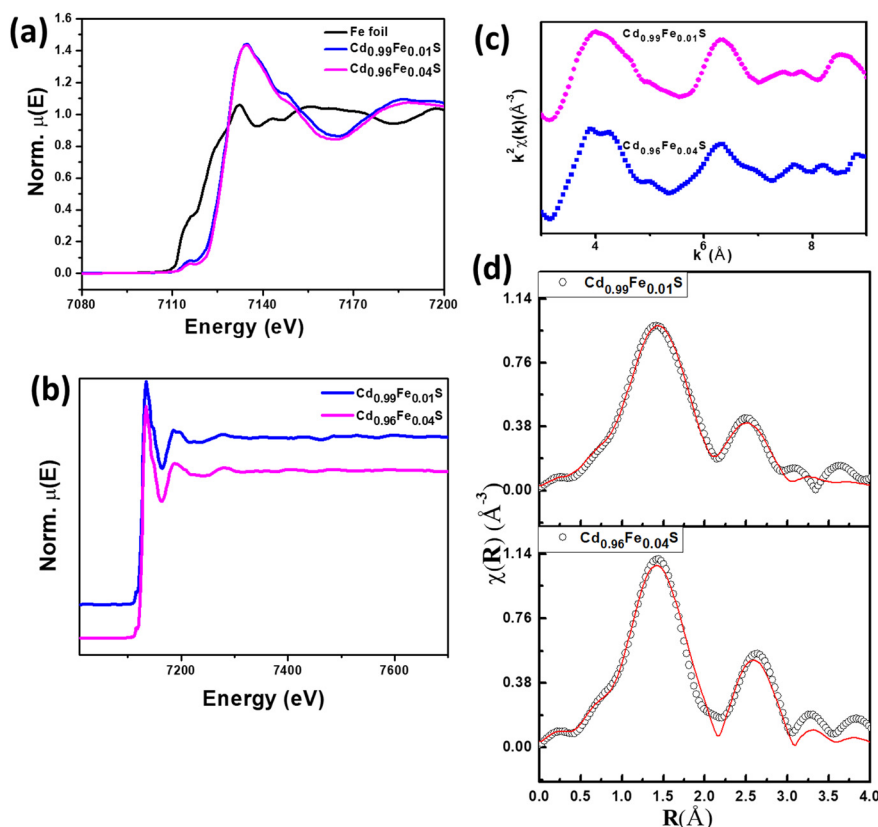
$$W(r) = \exp[r^2/2\sigma^2] \tag{5}$$

where σ is a constant that is matched individually with the sample's dimension.[62] Raman spectra of low-dimensional QDs become modified compared to their bulk counterparts. The FWHM of 1-LO decreases non-linearly with higher doping concentrations (Fig. 6c), which may be due to the local structural and vibrational disorder defects for Fe doping in the CdS host. The intensity of all the longitudinal optical modes (LO) rapidly decreases with increasing Fe concentration in CdS (Fig. 6d). The decrease in intensity occurs because of the microscopic structural disorder in the CdS lattice induced by Fe doping. The number of Cd–S–Cd bonds is decreased, and new Cd–S–Fe or Fe–S–Fe bonds are formed due to Cd substitution by Fe. As a result, the intensity of LO modes decreases with increasing Fe concentrations.[71] The decrease of relative Raman intensity in higher order longitudinal optical modes (LO) is ascribed to the weak exciton–phonon coupling (less than 1) shown in Fig. 6e due to small size of the QDs. Higher-order phonon overtones are observed under resonance conditions. Fig. 6e shows the linear decrease of the exciton–phonon coupling strength

Table 2 Bond length, coordination number (C.N.) and disorder factor obtained using EXAFS fitting for $Cd_{0.99}Fe_{0.01}S$ and $Cd_{0.96}Fe_{0.04}S$ quantum dots at the Cd K-edge

Path	Parameter	$Cd_{0.99}Fe_{0.01}S$	$Cd_{0.96}Fe_{0.04}S$
Cd K edge			
Cd–S	R (Å) (2.52)	2.49 ± 0.004	2.49 ± 0.002
	$N(4)$	3.77 ± 0.1	3.59 ± 0.07
	σ^2	0.0057 ± 0.0006	0.0056 ± 0.0003
	R_{factor}	0.009	0.003

© 2025 The Author(s). Published by the Royal Society of Chemistry

RSC Appl. Interfaces, 2025, **2**, 952–964 | **957**

Fig. 5 (a) Normalized XANES spectra of $Cd_{0.99}Fe_{0.01}S$ and $Cd_{0.96}Fe_{0.04}S$ along with standard at the Fe K-edge, (b) normalized absorption spectra, (c) normalised EXAFS ($k^2\chi(k)$ vs. k) spectra, and (d) Fourier-transformed EXAFS spectra of $Cd_{0.99}Fe_{0.01}S$ and $Cd_{0.96}Fe_{0.04}S$ quantum dots at the Fe K-edge. In (d), the black colored scatter points represent experimental spectra, and the red colored solid line represents the theoretical fit.

(I_{2LO}/I_{1LO}) of the prepared quantum dots with increasing Fe doping concentrations. The ratio of intensities of the overtone peaks to that of the most prominent peaks is related to the strength of the exciton–phonon interaction.[72,73]

3.5. UV-vis spectroscopy and photoluminescence spectroscopy

Fig. 7a and b show the reflectance and absorbance spectra of direct band gap undoped and Fe-doped CdS quantum

Table 3 Bond length, coordination number (C.N.) and disorder factor obtained using EXAFS fitting for $Cd_{0.99}Fe_{0.01}S$ and $Cd_{0.96}Fe_{0.04}S$ quantum dots at the Fe K-edge

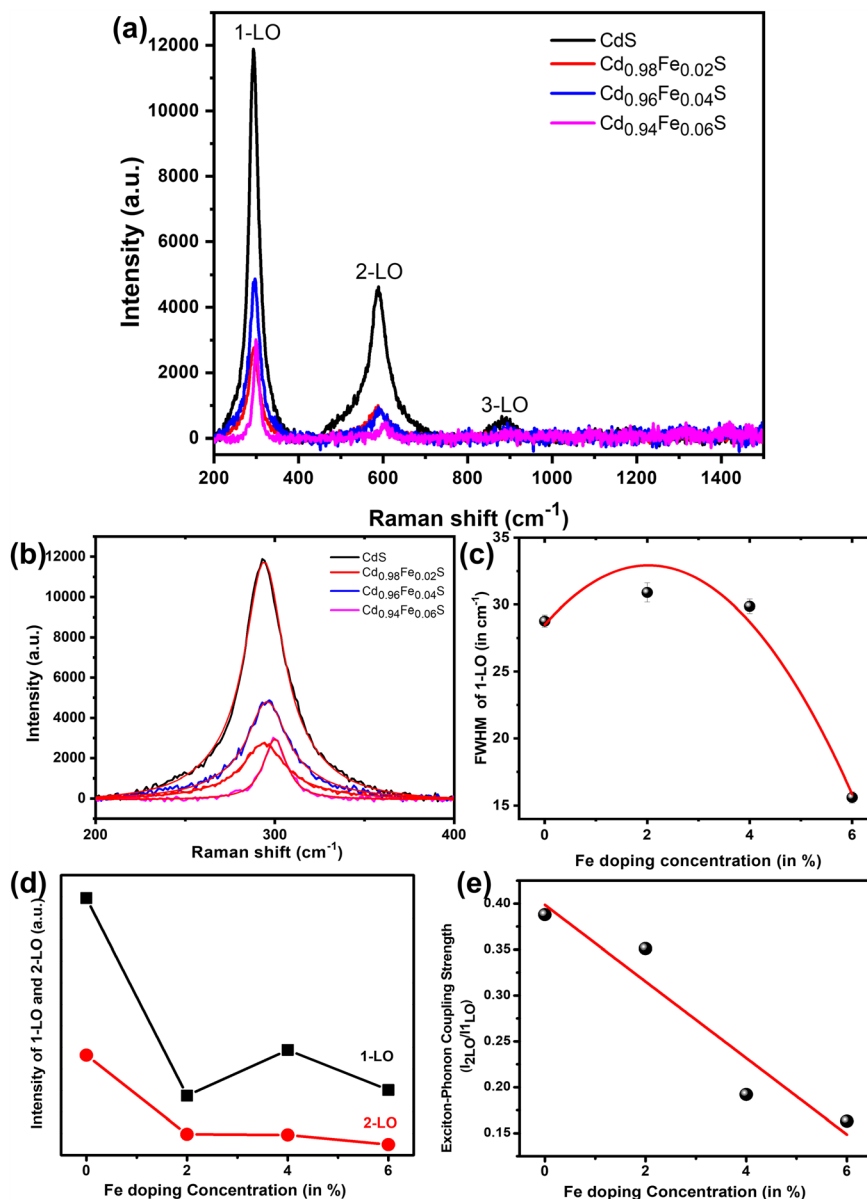| Path	Parameter	$Cd_{0.99}Fe_{0.01}S$	$Cd_{0.96}Fe_{0.04}S$
Fe K-edge			
Fe–S$_1$	R (Å) (1.94)	1.91 ± 0.002	1.90 ± 0.002
	$N(3)$	3.0 ± 0.18	2.68 ± 0.08
	σ^2	0.0042 ± 0.0004	0.001
Fe–S$_2$	R (Å) (2.11)	2.08 ± 0.002	2.07 ± 0.002
	$N(3)$	3.0 ± 0.18	2.68 ± 0.08
	σ^2	0.0042 ± 0.0004	0.001
Fe–Fe	R (Å) (2.97)	2.98 ± 0.003	3.01 ± 0.01
	$N(4)$	4.0 ± 0.24	3.57 ± 0.1
	σ^2	0.0172 ± 0.0014	0.0097 ± 0.0004
	R_{factor}	0.01	0.02

dots, respectively. Fig. 7c shows Tauc's plot for calculating the band gap. The band gaps have been calculated from the absorbance data using the Kubelka–Munk function.[55] The inset of Fig. 7c shows the band gap variation of Fe-doped CdS. The reason behind the band gap variation is quantum confinement arising from the smaller size of QDs due to Fe doping which is consistent with average crystallite size variation. The obtained band gaps are 2.348 eV, 2.404 eV, 2.318 eV, 2.216 eV, and 2.022 eV for Fe doping at 0%, 1%, 2%, 4%, 6%, and 8%, respectively. The initial slight increase in the bandgap from 2.348 eV (Fe = 0%) to 2.404 eV (Fe = 1%) can be attributed to the Moss–Burstein effect, where the introduction of Fe^{3+} ions from Fe-precursor leads to an enhancement in carrier concentration. This enhancement in carrier concentration pushes the Fermi level towards the conduction band. This effectively helps widen the optical bandgap as a result of occupying the lower energy states in the conduction band. However, the bandgap begins to decrease with the further increase of Fe-concentration. This can be attributed to the creation of localized states within the bandgap, as a result of the interaction of Fe^{3+} ions with the host CdS. These localized states act as trap states which lead to band tailing and lowered bandgaps.

The photoluminescence spectra have been measured to determine the luminescence properties and defect states present

Fig. 6 (a) Raman spectra of $Cd_{1-x}Fe_xS$ quantum dots at room temperature, (b) Raman spectra of $Cd_{1-x}Fe_xS$ quantum dots: 1-LO (fitted to get the exact peak position), (c) FWHM variation (1-LO) with Fe doping concentrations, (d) relative Raman intensity of 1-LO with increasing Fe doping concentrations, (e) variation in exciton–phonon coupling strength with Fe doping concentration.

in the samples. For this measurement, a fixed concentration of 1 mg sample/5 mL isopropanolic solution was maintained. The room-temperature photoluminescence spectra of undoped and Fe-doped CdS quantum dots (Fig. 8) indicate that the green luminescence peak near 530 nm increases with the doping

Table 4 Peak position (cm^{-1}) of nLO bands of undoped and Fe-doped CdS QDs (peak positions were obtained by fitting the bands)

	$n = 1$	$n = 2$	$n = 3$
CdS	294	588	885
CdS:Fe2	295	589	894
CdS:Fe4	296	596	894
CdS:Fe6	300	603	894

concentration of Fe but suddenly falls in the 8% doped sample.[58] This may be due to the precipitation of the samples with higher Fe concentrations in isopropanol solution. The band edge emission wavelengths near 480 nm are consistent with the UV-vis absorbance wavelength. Additionally, higher doping levels introduce structural disorder and induce defects. This result corroborates with the UV measurement contributing to the observed reduction in the bandgap at higher Fe-concentrations.

3.6. Rectifying diode behavior: scanning tunneling microscopy (STM) study

Scanning tunneling microscopy (STM) is a unique technique based on tunneling which yields surface topographies in
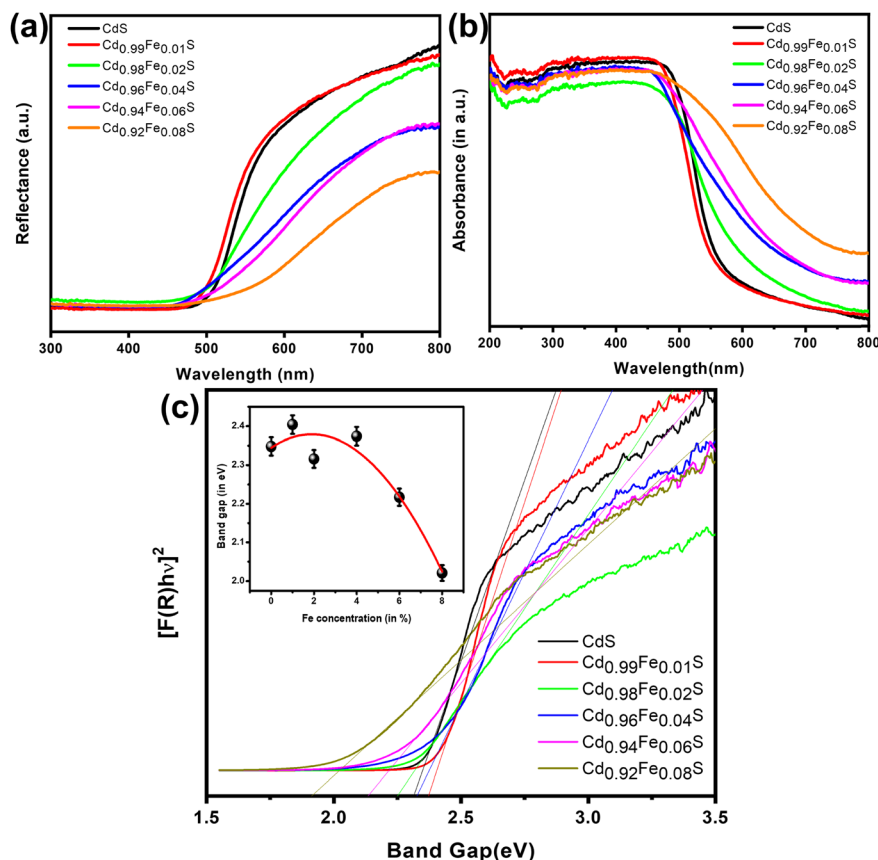
© 2025 The Author(s). Published by the Royal Society of Chemistry

RSC Appl. Interfaces, 2025, **2**, 952–964 | **959**

Fig. 7 (a) Reflectance spectra and (b) absorbance spectra of undoped and Fe-doped CdS quantum dots [$Cd_{1-x}Fe_xS$; Fe = 0%, 1%, 2%, 4%, 6%, and 8%]; (c) Tauc plots of undoped and Fe-doped CdS quantum dots (inset: band gap variation with Fe doping concentration).

real space and on an atomic scale. In this study, scanning tunneling spectroscopy (STS) has been used for investigation of rectification properties of single-dot diodes. Measurements using STM were carried out at room temperature. For practical application, it is essential to gain

a high rectification ratio in single dot diodes and to modulate the performance of rectification. For single-molecule devices, the structure of the quantum dot has a significant impact on whether the molecular current exhibits rectification phenomenon. This idea will be addressed in other work. This study mainly focused on the mechanisms of rectification in single dot diodes and the efficient ways to modulate their rectifying performance.

The schematic diagram of the device structure of the thin film single-dot rectifying diode has been displayed in Fig. 9a. Although, the schematic diagram is idealized using a very sharp tip in STM measurements, the ideal situation was nearly achieved. The current–voltage mechanism of device structure ITO/TiO_2/CdS:Fe QDs has been measured by scanning tunneling microscopy at ambient atmosphere with a Pt/Ir tip. The TiO_2 nano-powders were sonicated in isopropanol and spin-coated. Then, this thin film was annealed at 350 °C to obtain good crystallinity and phase formation. On the top of that layer, a single layer of Fe-doped CdS quantum dots was spin coated. Single dot devices with wide band gap TiO_2 were fabricated for rectifying diodes due to their ambient atmosphere stability and transparent properties.

The Pt/Ir tip for STM was used due to its high stability and conductivity in different types of measurements. Also, it has minimal reactivity with the material during imaging and
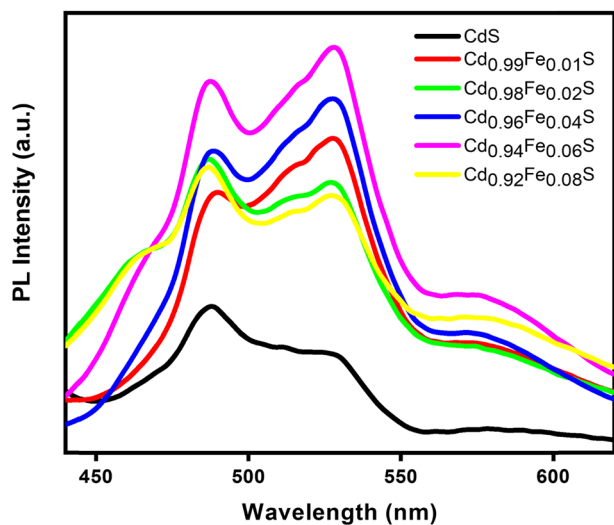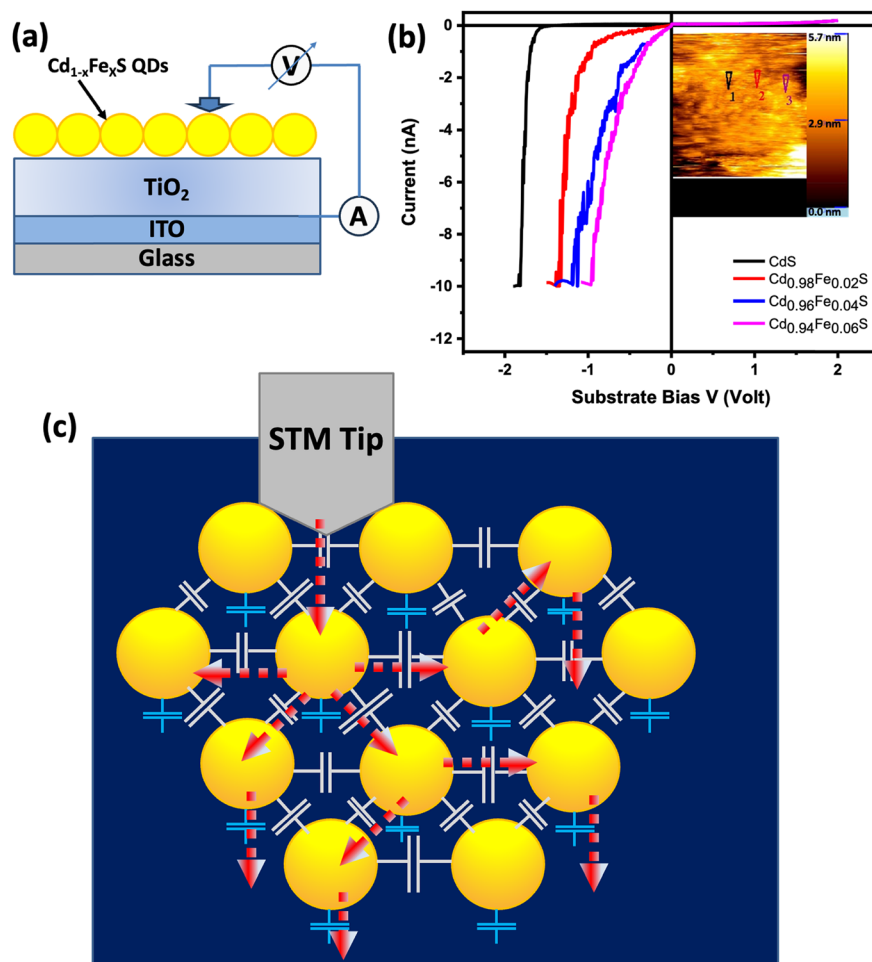

Fig. 8 Photoluminescence spectra of undoped and Fe-doped CdS [$Cd_{1-x}Fe_xS$] quantum dots.

Fig. 9 (a) Device structure of the ITO/TiO$_2$/Cd$_{1-x}$Fe$_x$S QDs rectifying diode [Fe = 0%, 2%, 4%, and 6%] and (b) rectifying behaviors of undoped and Fe-doped CdS single quantum dots (inset shows the scanning tunneling micrograph of 2% Fe-doped CdS QDs). (c) Schematic of the model of collective transport phenomena in the device. The yellow spheres denote CdS QDs. The dashed red line with arrows illustrates the electron transport path.

spectral measurements. The Pt/Ir tip provides a stable and reliable interface between tip/material for high-resolution imaging and current–voltage measurements. However, the tip material can have an impact on the results in a contact-dependent device. The tip material could have indirect effects on the local electronic interaction between the tip and material, due to the work function of the tip. The work function of the tip can influence the contact barrier and the molecular states alignment with the Fermi level electrode.

The device has been characterized by an STM with an input current of 10 pA. The diode nature is observed from current–voltage plot (Fig. 9b) and the inset shows the image of the QDs surface. The tunneling current has been enhanced up to 10 nA, giving the rectification ratio 10^3. The threshold voltage decreases with doping concentration from 1.62 V (CdS) to 0.83 V (Cd$_{0.94}$Fe$_{0.06}$S) which makes it promising for low power consumption. In Fe-doped CdS QDs, the threshold voltage decreases due to the band gap decreasing with doping concentration. This may be attributed to the decrease of carrier concentration, which affects the energy band

bending, resulting in an increase in depletion region width.[74] At negative bias voltage to the substrate ITO, the holes transport through the valence band of CdS QD to TiO$_2$ and TiO$_2$ to ITO. This results in the high current in the STS data with turn-on voltage. For Fe-doped CdS QDs, holes transport through the additional Fe doping energy band (DB) near the valence band of CdS. As a result, the turn-on voltage gets lowered at higher doping concentration due to the broadening of this DB band. The negative tunneling current and negative substrate bias voltage indicates the hole tunneling. Moreover, the electron tunneling at positive substrate bias voltage is very negligible due to lack of electrons. The regions highlighted "1", "2", and "3" in Fig. 9b and TOC represent different positions of the 2% Fe-doped CdS QDs film.

The inset of Fig. 9b shows the image of dots of 2% Fe-doped CdS QDs. Slight vibration was experienced during the recording of images, which might be attributed to the magnetic behavior of Fe, which results in the unclear STM image of quantum dots.[74]

© 2025 The Author(s). Published by the Royal Society of Chemistry

RSC Appl. Interfaces, 2025, **2**, 952–964 | 961

As electron tunnels from the STM tip to the QD, it will tunnel to another QD having far less polarization charge in order to reduce the Coulomb charging energy (Fig. 9c). Compared to the tip-to-dot and dot-to-substrate capacitances, the inter-dot capacitance is two orders of magnitude more significant to have a smaller Coulomb charging energy.[75] The electron could tunnel to the nearest neighbor QD to reduce the high Coulomb charging energy in the CdS:Fe QD situated between the STM tip and the ITO substrate. As pointed out in the Middleton–Wingreen (MW) model, while Coulomb blockade can be observed when the series tunnel barriers are approximately equal, the Coulomb staircase requires asymmetric barriers so that multiple electrons or holes can be accumulated in the QD, with a low probability of tunneling out and a high probability of being replenished. A noticeable rectification of 10^3 was demonstrated using a Pt/Ir STM tip held at a constant position on the target dot. Fabricated devices showed consistent performance across multiple batches and with time, demonstrating their stability and repeatability. Although, the long-term stability or impact of environmental factors on QDs and rectifier diodes are important factors for the application in real-world single dot-based devices, the current study primarily focused on the initial performance and stability of the rectifying diodes under ambient atmospheric conditions (at normal temperature and pressure). The evaluation of the long-term stability and effects of environmental factors such as humidity and temperature fluctuations will be studied elsewhere.

4. Conclusions

We successfully characterized Fe-doped CdS quantum dots for application in inexpensive, solution-processed rectifying diodes using room-temperature scanning tunneling microscopy (STM). Cubic structures were confirmed using XRD and EXAFS. UV-vis spectra revealed the emergence of semiconductor behavior and a decrease in band gap upon Fe doping. Furthermore, conductance tunability of the CdS surface by individual dots was demonstrated. STM images showed that ITO/TiO$_2$/CdS:Fe offered a rectification ratio of 10^3 in the rectifying diode. The maximum current was 10 nA owing to the instrument limitation. Tuning the threshold voltage from 1.66 eV to 0.83 eV (which is very low) indicated that the Fe-doped CdS quantum dots are promising for different electronic and optoelectronic applications with low electrical power loss. This study offers limited information on the potential application of QDs in rectifying diodes as the primary focus is on their STM analysis. STM results provided critical information regarding current–voltage characteristics for understanding the local electronic structure and surface morphology of QDs, which were crucial factors to understand and validate the behavior of the rectifying diode at the nanoscale level.

This study contributes to understanding the fundamental properties of Fe-doped CdS quantum dots and offers a groundwork for their potential technological advancements in thin film rectifying diodes. The insights would provide a platform for further research aiming at utilizing the doped quantum dot-based rectifying diodes for improved device functioning and performance in many technological applications.

Data availability

The authors declare that all the data reported in this paper are available upon reasonable request.

Conflicts of interest

There are no conflicts to declare.

Acknowledgements

References

1 M.-Y. Li, S.-K. Su, H.-S. P. Wong and L.-J. Li, *Nature*, 2019, **567**, 169–170.
2 Z. Donhauser, B. Mantooth, K. Kelly, L. Bumm, J. Monnell, J. J. Stapleton, D. Price Jr, A. Rawlett, D. Allara and J. Tour, *Science*, 2001, **292**, 2303–2307.
3 I. Franco, C. B. George, G. C. Solomon, G. C. Schatz and M. A. Ratner, *J. Am. Chem. Soc.*, 2011, **133**, 2242–2249.
4 J. L. Zhang, J. Q. Zhong, J. D. Lin, W. P. Hu, K. Wu, G. Q. Xu, A. T. Wee and W. Chen, *Chem. Soc. Rev.*, 2015, **44**, 2998–3022.
5 I. Díez-Pérez, J. Hihath, Y. Lee, L. Yu, L. Adamska, M. A. Kozhushner, I. I. Oleynik and N. Tao, *Nat. Chem.*, 2009, **1**, 635–641.
6 B. Capozzi, J. Xia, O. Adak, E. J. Dell, Z.-F. Liu, J. C. Taylor, J. B. Neaton, L. M. Campos and L. Venkataraman, *Nat. Nanotechnol.*, 2015, **10**, 522–527.
7 R. M. Metzger, *Chem. Rev.*, 2015, **115**, 5056–5115.
8 J. Park, A. N. Pasupathy, J. I. Goldsmith, C. Chang, Y. Yaish, J. R. Petta, M. Rinkoski, J. P. Sethna, H. D. Abruña and P. L. McEuen, *Nature*, 2002, **417**, 722–725.
9 T. V. de Medeiros, A. Macina, J. P. de Mesquita and R. Naccache, *RSC Appl. Interfaces*, 2024, **1**, 86–97.
10 R. E. Castellanos-Pineda, A. Baron-Jaimes, M. A. Millán-Franco, M. E. Rincón and O. A. Jaramillo-Quintero, *RSC Appl. Interfaces*, 2024, **1**, 741–747.
11 L.-H. Lai, W.-H. Lin, C.-C. Hsieh and M. A. Loi, *RSC Appl. Interfaces*, 2024, **1**, 122–132.
12 L. Sun, Y. A. Diaz-Fernandez, T. A. Gschneidtner, F. Westerlund, S. Lara-Avila and K. Moth-Poulsen, *Chem. Soc. Rev.*, 2014, **43**, 7378–7411.

962 | *RSC Appl. Interfaces*, 2025, **2**, 952–964

© 2025 The Author(s). Published by the Royal Society of Chemistry

13 F. Wu, H. Tian, Z. Yan, J. Ren, T. Hirtz, G. Gou, Y. Shen, Y. Yang and T.-L. Ren, *ACS Appl. Mater. Interfaces*, 2021, **13**, 26161–26169.

14 A. Yakimov, V. Kirienko, A. Bloshkin, A. Dvurechenskii and D. Utkin, *J. Phys. D: Appl. Phys.*, 2020, **53**, 335105.

15 D. J. Frank, R. H. Dennard, E. Nowak, P. M. Solomon, Y. Taur and H.-S. P. Wong, *Proc. IEEE*, 2001, **89**, 259–288.

16 G. Maruccio, R. Cingolani and R. Rinaldi, *J. Mater. Chem. C*, 2004, **14**, 542–554.

17 Y. Zhang, D. Tu, L. Wang, C. Li, Y. Liu and X. Chen, *Mater. Chem. Front.*, 2024, **8**, 192–209.

18 D. Xiang, X. Wang, C. Jia, T. Lee and X. Guo, *Chem. Rev.*, 2016, **116**, 4318–4440.

19 T. Li, W. Hu and D. Zhu, *Adv. Mater.*, 2010, **22**, 286–300.

20 M. A. Reed, C. Zhou, C. Muller, T. Burgin and J. Tour, *Science*, 1997, **278**, 252–254.

21 D. Xiang, H. Jeong, T. Lee and D. Mayer, *Adv. Mater.*, 2013, **25**, 4845–4867.

22 X. Cui, A. Primak, X. Zarate, J. Tomfohr, O. Sankey, A. Moore, T. Moore, D. Gust, G. Harris and S. Lindsay, *Science*, 2001, **294**, 571–574.

23 S. Ho Choi, B. Kim and C. D. Frisbie, *Science*, 2008, **320**, 1482–1486.

24 W. Liang, M. P. Shores, M. Bockrath, J. R. Long and H. Park, *Nature*, 2002, **417**, 725–729.

25 B. Xu and N. J. Tao, *Science*, 2003, **301**, 1221–1223.

26 L. Venkataraman, J. E. Klare, C. Nuckolls, M. S. Hybertsen and M. L. Steigerwald, *Nature*, 2006, **442**, 904–907.

27 X. Guo, J. P. Small, J. E. Klare, Y. Wang, M. S. Purewal, I. W. Tam, B. H. Hong, R. Caldwell, L. Huang and S. O'brien, *Science*, 2006, **311**, 356–359.

28 Y. Cao, S. Dong, S. Liu, L. He, L. Gan, X. Yu, M. L. Steigerwald, X. Wu, Z. Liu and X. Guo, *Angew. Chem.*, 2012, **124**, 12394–12398.

29 J. Tang, Y. Wang, J. E. Klare, G. S. Tulevski, S. J. Wind and C. Nuckolls, *Angew. Chem.*, 2007, **119**, 3966–3969.

30 S. Kubatkin, A. Danilov, M. Hjort, J. Cornil, J.-L. Bredas, N. Stuhr-Hansen, P. Hedegård and T. Bjørnholm, *Nature*, 2003, **425**, 698–701.

31 H. B. Akkerman, P. W. Blom, D. M. De Leeuw and B. De Boer, *Nature*, 2006, **441**, 69–72.

32 N. J. Tao, *Nat. Nanotechnol.*, 2006, **1**, 173–181.

33 S. V. Aradhya and L. Venkataraman, *Nat. Nanotechnol.*, 2013, **8**, 399–410.

34 K. Moth-Poulsen and T. Bjørnholm, *Nat. Nanotechnol.*, 2009, **4**, 551–556.

35 S. M. Lindsay and M. A. Ratner, *Adv. Mater.*, 2007, **19**, 23–31.

36 C. Lambert, *Chem. Soc. Rev.*, 2015, **44**, 875–888.

37 C. M. Guédon, H. Valkenier, T. Markussen, K. S. Thygesen, J. C. Hummelen and S. J. Van Der Molen, *Nat. Nanotechnol.*, 2012, **7**, 305–309.

38 S. Ballmann, R. Härtle, P. B. Coto, M. Elbing, M. Mayor, M. R. Bryce, M. Thoss and H. B. Weber, *Phys. Rev. Lett.*, 2012, **109**, 056801.

39 C. Jia, A. Migliore, N. Xin, S. Huang, J. Wang, Q. Yang, S. Wang, H. Chen, D. Wang and B. Feng, *Science*, 2016, **352**, 1443–1445.

40 Z. Liu, S. Ren and X. Guo, *Molecular-Scale Electronics: Current Status and Perspectives*, 2017, pp. 173–205.

41 P. Reddy, S.-Y. Jang, R. A. Segalman and A. Majumdar, *Science*, 2007, **315**, 1568–1571.

42 D. Nozaki, S. M. Avdoshenko, H. Sevincli and G. Cuniberti, *J. Appl. Phys.*, 2014, **116**, 074308.

43 M. Elbing, R. Ochs, M. Koentopp, M. Fischer, C. von Hänisch, F. Weigend, F. Evers, H. B. Weber and M. Mayor, *Proc. Natl. Acad. Sci. U. S. A.*, 2005, **102**, 8815–8820.

44 W. Y. Kim and K. S. Kim, *Acc. Chem. Res.*, 2010, **43**, 111–120.

45 S. Sanvito, *Chem. Soc. Rev.*, 2011, **40**, 3336–3355.

46 X. Guo, *Adv. Mater.*, 2013, **25**, 3397–3408.

47 Y. Zhao, B. Ashcroft, P. Zhang, H. Liu, S. Sen, W. Song, J. Im, B. Gyarfas, S. Manna and S. Biswas, *Nat. Nanotechnol.*, 2014, **9**, 466–473.

48 J. Wang, F. Shen, Z. Wang, G. He, J. Qin, N. Cheng, M. Yao, L. Li and X. Guo, *Angew. Chem.*, 2014, **126**, 5138–5143.

49 G. He, J. Li, H. Ci, C. Qi and X. Guo, *Angew. Chem.*, 2016, **128**, 9182–9186.

50 M. Hawley, I. D. Raistrick, J. G. Beery and R. J. Houlton, *Science*, 1991, **251**, 1587–1589.

51 P. Vancsó, G. Z. Magda, J. Pető, J.-Y. Noh, Y.-S. Kim, C. Hwang, L. P. Biró and L. Tapasztó, *Sci. Rep.*, 2016, **6**, 29726.

52 A. Aviram, C. Joachim and M. Pomerantz, *Chem. Phys. Lett.*, 1988, **146**, 490–495.

53 C. Joachim, J. K. Gimzewski, R. R. Schlittler and C. Chavy, *Phys. Rev. Lett.*, 1995, **74**, 2102.

54 A. Zhao, Q. Li, L. Chen, H. Xiang, W. Wang, S. Pan, B. Wang, X. Xiao, J. Yang and J. Hou, *Science*, 2005, **309**, 1542–1544.

55 T. Komeda, H. Isshiki, J. Liu, Y.-F. Zhang, N. Lorente, K. Katoh, B. K. Breedlove and M. Yamashita, *Nat. Commun.*, 2011, **2**, 217.

56 S. Schmaus, A. Bagrets, Y. Nahas, T. K. Yamada, A. Bork, M. Bowen, E. Beaurepaire, F. Evers and W. Wulfhekel, *Nat. Nanotechnol.*, 2011, **6**, 185–189.

57 S. Kahle, Z. Deng, N. Malinowski, C. Tonnoir, A. Forment-Aliaga, N. Thontasen, G. Rinke, D. Le, V. Turkowski and T. S. Rahman, *Nano Lett.*, 2012, **12**, 518–521.

58 P. Maity, S. Kumar, R. Kumar, S. Jha, D. Bhattacharyya, S. Barman, S. Chatterjee, B. N. Pal and A. K. Ghosh, *J. Phys. Chem. C*, 2021, **125**, 2074–2088.

59 P. Maity, S. V. Singh, S. Biring, B. N. Pal and A. K. Ghosh, *J. Mater. Chem. C*, 2019, **7**, 7725–7733.

60 B. Prajapati, S. Kumar, M. Kumar, S. Chatterjee and A. K. Ghosh, *J. Mater. Chem. C*, 2017, **5**, 4257–4267.

61 J. Hwang, M. Pototschnig, R. Lettow, G. Zumofen, A. Renn, S. Götzinger and V. Sandoghdar, *Nature*, 2009, **460**, 76–80.

62 K. Boldt, S. Bartlett, N. Kirkwood and B. Johannessen, *Nano Lett.*, 2020, **20**, 1009–1017.

63 L. Haddad, D. Gianolio, D. J. Dunstan, Y. Liu, C. Rankine and A. Sapelkin, *Nanoscale*, 2024, **16**, 5768–5775.

64 K. A. Svit, A. A. Zarubanov, T. A. Duda, S. V. Trubina, V. V. Zvereva, E. V. Fedosenko and K. S. Zhuravlev, *Langmuir*, 2021, **37**, 5651–5658.

65 Y. Zhang, H. Zhang, D. Chen, C.-J. Sun, Y. Ren, J. Jiang, L. Wang, Z. Li and X. Peng, *Nano Lett.*, 2021, **21**, 5201–5208.

66 H. Richter, Z. Wang and L. Ley, *Solid State Commun.*, 1981, **39**, 625–629.

67 I. Campbell and P. M. Fauchet, *Solid State Commun.*, 1986, **58**, 739–741.

68 F. Comas and C. Trallero-Giner, *Phys. Rev. B: Condens. Matter Mater. Phys.*, 2003, **67**, 115301.

69 A. Singha, B. Satpati, P. Satyam and A. Roy, *J. Phys.: Condens. Matter*, 2005, **17**, 5697.

70 A. K. Arora, M. Rajalakshmi, T. Ravindran and V. Sivasubramanian, *J. Raman Spectrosc.*, 2007, **38**, 604–617.

71 K. Roodenko, I. Goldthorpe, P. McIntyre and Y. Chabal, *Phys. Rev. B: Condens. Matter Mater. Phys.*, 2010, **82**, 115210.

72 P. Maity, R. Kumar, S. Jha, D. Bhattacharyya, R. K. Singh, S. Chatterjee and A. K. Ghosh, *J. Mater. Sci.: Mater. Electron.*, 2022, **33**, 21822–21837.

73 A. Rolo and M. Vasilevskiy, *J. Raman Spectrosc.*, 2007, **38**, 618–633.

74 M. El-Hagary and S. Soltan, *J. Appl. Phys.*, 2012, **112**, 043907.

75 B. Paquelet Wuetz, D. Degli Esposti, A.-M. J. Zwerver, S. V. Amitonov, M. Botifoll, J. Arbiol, A. Sammak, L. M. Vandersypen, M. Russ and G. Scappucci, *Nat. Commun.*, 2023, **14**, 1385.